# Reconstructing subcortical and cortical somatosensory activity via the RAMUS inverse source analysis technique using median nerve SEP data

Atena Rezaei [a,*], Joonas Lahtinen [a], Frank Neugebauer [a,b], Marios Antonakakis [b,e], Maria Carla Piastra [c], Alexandra Koulouri [a], Carsten H. Wolters [b,d], Sampsa Pursiainen [a]

[a] *Faculty of Information and Communication Sciences, Unit of Computing Sciences, Tampere University, P.O. Box 1001, Tampere 33014, Finland*
[b] *Institute for Biomagnetism and Biosignalanalysis, University of Münster, Malmedyweg 15, Münster D-48149, Germany*
[c] *Cognitive Neuroscience, Donders Institute for Brain, Cognition and Behaviour, Radboud University Nijmegen Medical Centre, Kapittelweg 29, Nijmegen 6525 EN, the Netherlands*
[d] *Otto Creutzfeldt Center for Cognitive and Behavioral Neuroscience, University of Münster, Münster D-48149, Germany*
[e] *School of Electrical and Computer Engineering, Technical University of Crete, Akrotiri Campus Chania 73100, Crete, Greece*

## A R T I C L E   I N F O

## A B S T R A C T

This study concerns reconstructing brain activity at various depths based on non-invasive EEG (electroencephalography) scalp measurements. We aimed at demonstrating the potential of the RAMUS (randomized multiresolution scanning) technique in localizing weakly distinguishable far-field sources in combination with coinciding cortical activity. As we have shown earlier theoretically and through simulations, RAMUS is a novel mathematical method that by employing the multigrid concept, allows marginalizing noise and depth bias effects and thus enables the recovery of both cortical and subcortical brain activity. To show this capability with experimental data, we examined the 14–30 ms post-stimulus somatosensory evoked potential (SEP) responses of human median nerve stimulation in three healthy adult subjects. We aim at reconstructing the different response components by evaluating a RAMUS-based estimate for the primary current density in the nervous tissue. We present source reconstructions obtained with RAMUS and compare them with the literature knowledge of the SEP components and the outcome of the unit-noise gain beamformer (UGNB) and standardized low-resolution brain electromagnetic tomography (sLORETA). We also analyzed the effect of the iterative alternating sequential technique, the optimization technique of RAMUS, compared to the classical minimum norm estimation (MNE) technique. Matching with our previous numerical studies, the current results suggest that RAMUS could have the potential to enhance the detection of simultaneous deep and cortical components and the distinction between the evoked sulcal and gyral activity.

## 1. Introduction

The interest for detecting subcortical brain activity has been increasing in recent years since it could unlock new avenues for pathophysiological research which ultimately could lead to the treatment of brain disorders such as Alzheimer's disease (Laxton and Lozano, 2013) and Parkinson's disease (Obeso et al., 2008). Detecting the weak activity from deep brain structures is a challenging task as the source is far from the sensors on the scalp (Krishnaswamy et al., 2017). Recently, detecting the subcortical generators has been investigated by applying sparsity constraints (Krishnaswamy et al., 2017) in source domains and employing cortical signal suppression (CSS) (Samuelsson et al., 2019) utilizing non-invasive brain measurement, i.e., electroencephalography (EEG) and magnetoenecephalography (MEG). In this study, we aim to reconstruct both cortical and subcortical activity from the somatosensory evoked potential (SEP) of the human median nerve stimulation (Hari and Puce, 2017; Niedermeyer and da Silva, 2004; Rezaei et al., 2020b) based on non-invasive EEG scalp measurements by applying randomized multiresolution scanning (RAMUS) (Rezaei et al., 2020b) approach. Herein, we consider thalamus and brainstem as target subcortical structures due to their significant contribution in sensory processing (Jones, 2001; 2002; Krishnaswamy et al., 2017). RAMUS is a numerical technique to reduce the effect of optimization and discretization errors. The reconstruction process of RAMUS progresses gradually from coarse resolution to the finest one. Using a sparse source space is advantageous in reconstructing the activity from weak deep-lying sources (Krishnaswamy et al., 2017). RAMUS combines sampling and randomized lower and higher resolution projections of the candidate solution set (He et al., 2019; Rezaei et al., 2020b) to improve the detectability of the components located in the subcortical part of the brain and to obtain a high resolution or focality in the cortical areas without separate or suppressing the cortical activity (Samuelsson et al., 2019). In addi-

tion to several resolution levels, RAMUS utilizes multiple randomized source sets at each resolution level to enhance the noise-robustness of the reconstruction process. This process does not restrict or suppress any components of the source space, thereby, it distinguishes RAMUS from other approaches, e.g., the cortical signal suppression (CSS) technique (Samuelsson et al., 2019). Consequently, RAMUS can be interpreted as a technique to marginalize the effect of the noise and the source space, i.e., discretization errors, on the source localization algorithm, or as a generalization of that algorithm to multiple resolutions and source sets. Here, our aim is to investigate the potential advantages and limitations of the RAMUS in reconstructing the activity associated with the sequential latencies of human median nerve SEPs.

In Rezaei et al. (2020b), RAMUS was suggested to be a potential technique to detect deep activity and to distinguish simultaneous cortical and subcortical components. RAMUS relies on a hierarchical Bayesian model (HBM) combining a conditionally Gaussian prior and the inverse gamma (IG) hyperprior, i.e., the conjugate hyperprior (Calvetti et al., 2009; Lucka et al., 2012). Using this combination, we have previously simulated the capability of RAMUS to distinguish a subcortical activity component both individually and when coupled with a cortical one (Götz et al., 2014; Haueisen et al., 2007; Rezaei et al., 2020b). This situation occurs at 14 and 20 ms post-stimulus in response to the stimulus of the human median nerve (Rezaei et al., 2020b). Here we aim to show this with experimental data to reconstruct different response components which occur 14–30 ms post-stimulus, consecutively, whereas previous studies focused on reconstructing the simultaneous activity of post-stimulus responses of a single time course (Krishnaswamy et al., 2017). The aforementioned components involve both subcortical and cortical activity as the afferent volley travels from the median nerve to the cervical spine, continuing through the subcortical region, i.e., brainstem and thalamus, to the cortical structures. We consider an approach to estimate the primary current distribution in the nervous tissue. Furthermore, we have included numerical experiments for P14/N14 and P20/N20 components to verify the consistency of our results with the experimental datasets for three subjects. In addition to the RAMUS technique, reconstructions were obtained by unit-noise gain beamformer (UNGB) (Sekihara and Nagarajan, 2008) and standardized low-resolution brain electromagnetic tomography (sLORETA) (Pascual-Marqui, 2002) for the aforementioned latencies to assess the performance of RAMUS compared with alternative inverse approaches with respect to the reconstructed activity for both subcortical and cortical domains.

In general, finding the primary current distribution poses an ill-posed and ill-conditioned inverse problem (Kaipio and Somersalo, 2004), i.e., a non-uniquely solvable problem which is vulnerable to measurement or modelling uncertainties. The feasibility of detecting the subcortical activity as a distribution based on non-invasive electric potential or magnetic field measurements has been shown recently (Andersen et al., 2020; Attal and Schwartz, 2013; Krishnaswamy et al., 2017; Pizzo et al., 2019; Samuelsson et al., 2019; Seeber et al., 2019). Various other optimization-based and Bayesian approaches to the source localization problem exist, e.g., studies by Sommariva and Sorrentino (2014) and Gramfort et al. (2012). These however, do not consider the present strategy of decomposing the source space directly into randomized sets and multiple resolution levels which is motivated by the general sensitivity analysis for inverse problems, see, e.g., Pursiainen (2008); Rezaei et al. (2020b). The rationale of our present approach are the following: (i) There is a comparably broad literature available on the originators of the peaks investigated (Buchner et al., 1995a; 1994; 1997; 1995b; Curio et al., 1997; Gobbelé et al., 1998; Götz et al., 2014; Hari et al., 2018; Haueisen et al., 2007; Nakamura et al., 1998; Noël et al., 1996; Urasaki et al., 1990); (ii) as the numerical reference, we examine synthetic dipolar sources associated with the originators of the 14 and 20 ms peaks; (iii) the data acquired for human subjects allows us to investigate whether the mathematical and numerical basis of RAMUS is valid in the presence of modelling error and noise related to an exper-

imental measurement, especially, regarding the weakly distinguishable far-field components; (iv) our method to analyze multiple components allows approaching the source localization task as a sequential process which is important from the viewpoint of potential connectivity analysis applications, where the capability to localize the primary current distribution accurately is a prerequisite (Antonakakis et al., 2019; Buchner et al., 1994; Hari et al., 2018).

We present the reconstructions obtained with RAMUS technique and compare them with the literature knowledge of the SEP components as well as with the outcome of UNGB and sLORETA. We also analyze the effect of the iterative alternating sequential (IAS) method, the optimization technique of RAMUS, compared to the classical minimum norm estimate (MNE) (Hämäläinen and Ilmoniemi, 1994), examining the performance MNE-RAMUS, wherein the MAP estimation process of RAMUS is carried out via MNE instead of IAS as an optimization algorithm. Matching with our previous numerical results presented in (Rezaei et al., 2020b), the findings of this study suggest that RAMUS enhances the detection of simultaneous near- and far-field components, and in the former case, the distinction of the evoked sulcal and gyral activity.

This study is structured as follows. In Section 2.4, we briefly review the investigated SEP components, the literature on their anatomical origin, and describe the data, experiments, and implementation. Section 3 presents the results and Section 4 includes the discussion. A brief mathematical description of the RAMUS technique can be found in Section 2.3.

## 2. Materials and methods

### 2.1. Theoretical background

We utilize the linear forward model of EEG, where the measurement vector $\mathbf{y}$ depends on the unknown discretized primary current distribution $\mathbf{x}$ as given by Eqn 1

$$\mathbf{y} = \mathbf{L}\mathbf{x} + \mathbf{n} \tag{1}$$

where $\mathbf{n}$ is a Gaussian measurement noise term and $\mathbf{L}$ is the lead field matrix which can be obtained via quasi-static approximation of the Maxwell's equations and the finite element method as shown, for example, in Miinalainen et al. (2019). To reconstruct $\mathbf{x}$ given $\mathbf{y}$, we use the HBM in which the *a posteriori* probability of observing $\mathbf{x}$ is

$$\pi(\mathbf{x}, \theta \mid \mathbf{y}) \propto \pi(\theta)\pi(\mathbf{x} \mid \theta)\,\pi(\mathbf{y} \mid \mathbf{x}). \tag{2}$$

Here, in Eqn 2 $\pi(\mathbf{y} \mid \mathbf{x})$ is a Gaussian likelihood, i.e., the probability of measuring $\mathbf{y}$ given $\mathbf{x}$, and $\pi(\mathbf{x} \mid \theta)$ is a zero-mean conditionally Gaussian *a priori* probability with independent components. Its variance is given by the entries of the hyperparameter $\theta$ distributed according to the hyperprior $\pi(\theta)$. For the hyperprior, we use the inverse gamma distribution which is determined by the shape and scale parameters $\beta$ and $\theta_0$. As the hyperprior is heavy-tailed, some of the entries of $\mathbf{x}$ are likely to have a considerably large absolute value compared to the expectation. Consequently, the primary current distribution presented by $\mathbf{x}$ is likely to be focal. The shape parameter controls the weight of the tail: the smaller the value, the heavier the tail and the more focal $\mathbf{x}$. The expectation $\theta_0/(\beta - 1)$ of the hyperprior can be interpreted as the baseline variance of the conditional Gaussian prior (Calvetti et al., 2009). Thus, the square root of the expectation $\sqrt{\theta_0/(\beta - 1)}$ sets the expected (noise) amplitude for the entries of $\mathbf{x}$.

### 2.2. IAS algorithm

To maximize the posterior, we use the iterating alternating sequential (IAS) *maximum a posteriori* algorithm. In IAS, the number of iteration steps and the initial prior variance $\theta^{(0)} = (\theta_0, \theta_0, \dots, \theta_0)$ are the first set. Then, the estimates for $\mathbf{x}$ and $\theta$ are updated alternatingly as follows in
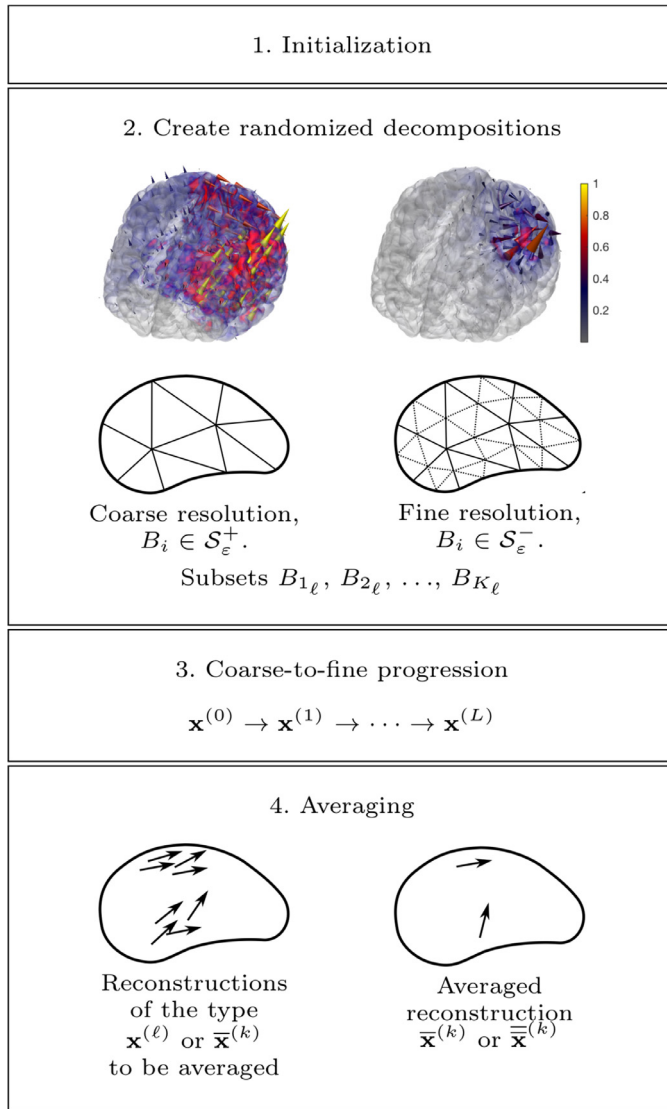
**Fig. 1.** RAMUS algorithm with a schematic illustrations of its steps. Visualization of vector field reconstructions (cones) for two different resolutions. Coarse resolution corresponds to less variability in the cone orientations and a greater dispersion of the amplitude due to fewer number of source locations.

Eqn 3

$$\mathbf{x}_{j+1} = \arg\max_{\mathbf{x}} \pi(\mathbf{x} \mid \boldsymbol{\theta}_j),$$
$$\boldsymbol{\theta}_{j+1} = \arg\max_{\boldsymbol{\theta}} \pi(\boldsymbol{\theta} \mid \mathbf{x}_{j+1}). \tag{3}$$

### 2.3. RAMUS algorithm

RAMUS decomposes the source space progressing from coarse resolution levels towards finer ones to enable reconstructing the weakly distinguishable (ill-conditioned) part of the source space (Pursiainen, 2008), here, especially, referring to the subcortical activity. In addition to this resolution progression, RAMUS averages the estimate over several randomized source sets, for each resolution level, in order to obtain the best reliability of the results. Below, we describe the steps of the RAMUS algorithm also illustrated in Fig. 1. For a more detailed description, see Rezaei et al. (2020b).

*Initialization* Choose the desired number of resolution levels $L$ and the sparsity factor (the ratio of the source counts) $s$ between each level. The number of sources at a given resolution level will be $K_\ell = K s^{(\ell - L)}$,

where $\ell = 1, 2, \ldots, L$ is the index of the resolution level, the larger the value of the index $\ell$ the finer the resolution.

*Create randomized decompositions* Generate a desired number $D$ of independent multiresolution decompositions $\mathfrak{S}_1, \mathfrak{S}_2, \ldots, \mathfrak{S}_D$ each consisting of sequentially generated resolution levels from 1 to $L$. For each resolution level $\ell = 1, 2, \ldots, L$, create a random uniformly distributed set of center points $\vec{p}_1, \vec{p}_2, \ldots, \vec{p}_{K_\ell}$ within the active brain tissue. Find source point subsets $B_1, B_2, \ldots, B_{K_\ell}$ applying the nearest point interpolation scheme with respect to the center points. Each subset $B_j$ consists of those source positions of the total source space $S$, whose nearest neighbor with respect to $\vec{p}_1, \vec{p}_2, \ldots, \vec{p}_{K_\ell}$ is $\vec{p}_j$. The average number of source positions associated with $B_j$ is approximately given by the sparsity factor $s$. The resolution of this subdivision grows along with the number of the center points (Fig. 1). The unknown parameter in is assumed to be constant in each subset, and the total source count in subsets $B_1, B_2, \ldots, B_{K_\ell}$ is equal to that of the original set. A sparse enough subset will belong to the set of detectable $S_\varepsilon^+ = \{\mathbf{x} : \|\mathbf{L}\mathbf{x}\| \geq \varepsilon \|\mathbf{x}\|\}$ while in a denser one it might belong to $S_\varepsilon^- = \{\mathbf{x} : \|\mathbf{L}\mathbf{x}\| < \varepsilon \|\mathbf{x}\|\}$.

*Coarse-to-fine progression* Start the reconstruction process with the decomposition $\mathfrak{S}_1$ and a suitably chosen initial guess $\mathbf{x}^{(0)}$. For decomposition $\mathfrak{S}_k$, find a reconstruction $\mathbf{x}^{(\ell)}$ with the IAS MAP technique with the initial guess $\mathbf{x}^{(\ell-1)}$ for the resolution levels $\ell = 1, 2, \ldots, L$.

*Averaging* After going through all decompositions, obtain the final estimate for the decomposition (basis) $k$ as the normalized mean

$$\overline{\mathbf{x}}^{(k)} = \sum_{\ell=1}^{L} \mathbf{x}^{(\ell)} \Big/ \sum_{\ell=1}^{L} s^{(L-\ell)}, \tag{4}$$

where in Eqn 4 the denominator is to balance the effect of the multiplied source count following from the interpolation of a coarse level estimate to a denser resolution level. If $k < D$, move to the next decomposition, i.e., update $k \to k + 1$, and repeat the previous step with the initial guess $\overline{\mathbf{x}}^{(k-1)}$ for the resolution level $\ell = 1$. Otherwise, obtain the final reconstruction as the mean:

$$\overline{\overline{\mathbf{x}}}^{(k)} = \frac{1}{D} \sum_{k=1}^{D} \overline{\mathbf{x}}^{(k)}.$$

With RAMUS, we expect to minimize both random optimization and discretization effects as suggested in Rezaei et al. (2020b). We update the initial guess to obtain the best possible MAP estimate for each source space. Assuming that the optimization process is ideal, the discretization effects may be approximated as independently and identically distributed and, thus, asymptotically Gaussian with a variance which tends to zero as $O(D^{-1/2})$.

Technically, this process is equivalent to first evaluating the mean for each resolution level and then normalizing that over different resolutions. Since the final reconstruction is obtained as a mean over all reconstruction levels, the potential systematic discretization errors also will be averaged with equal weighting. This approach is used, since different resolution levels localize different details. Consequently, the details found for most of the levels are likely to gain the greatest intensity in the final reconstruction.

### 2.4. Somatosensory evoked potentials (SEP)

We study the SEP components occurring between 14 and 30 ms post-stimulus. Of these, the earlier components, i.e., at 14–18 ms consist of deep activity including different parts of the brainstem and the thalamus. In addition to the deep activity, the responses between 20 and 30 ms include cortical contributions which represent the maximum peak of each corresponding component (Cebolla et al., 2011; Haueisen et al., 2007; Papadelis et al., 2011). The SEP components include positive (P) and negative (N) peaks characteristic to a given measurement configuration and reference which is conventionally the forehead potential (Buchner et al., 1995a; 1994). The reconstruction outcome is invariant with respect to the reference, i.e., the positive and negative polarity of the data. The components investigated are described below
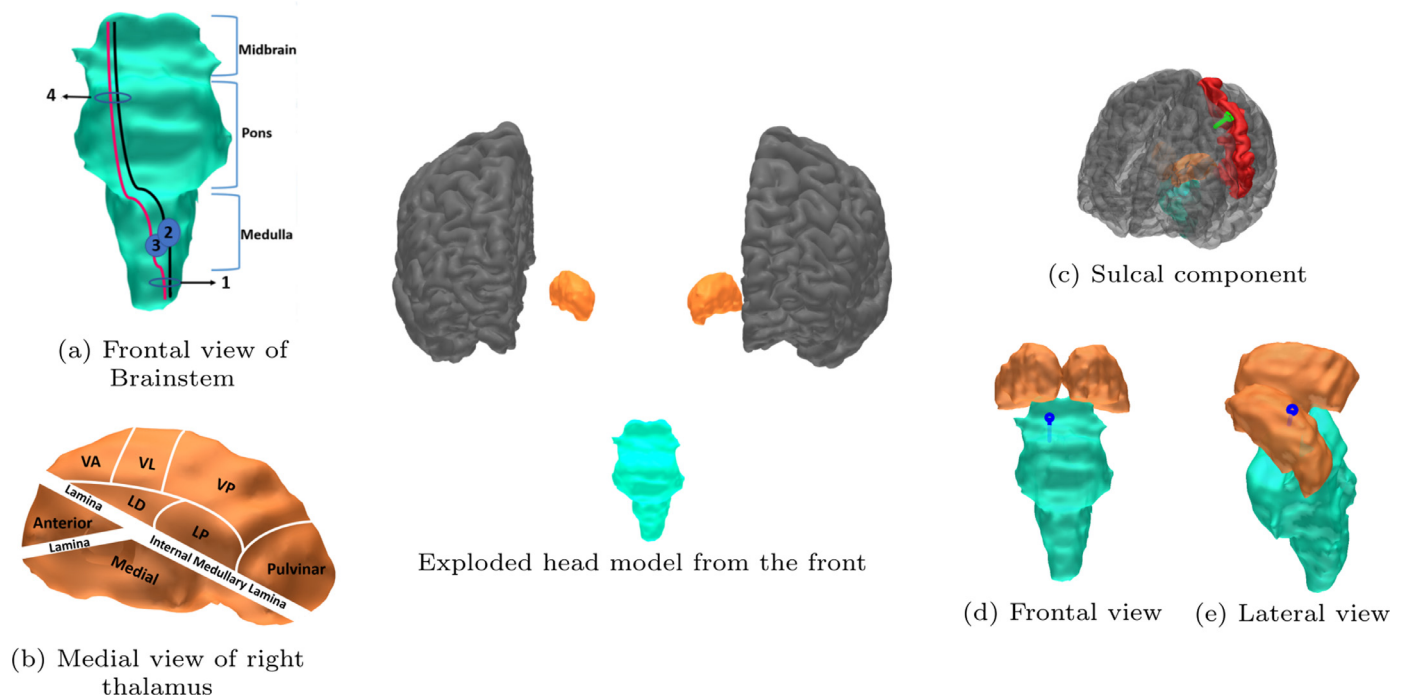
(a) Frontal view of Brainstem

(b) Medial view of right thalamus

Exploded head model from the front

(c) Sulcal component

(d) Frontal view  (e) Lateral view

**Fig. 2.** A visualization of brainstem and thalamus and different source configurations of synthetic source for P14/N14 and P20/N20 components. (a) displays different parts of the brainstem such as midbrain, pons and medulla. Label 1 illustrates the *dorsal column* pathway. Label 2 and 3 refer to *nucleus cuneatus* and *nucleus gracilis*, respectively. Label 4 depicts the *medial lemniscus* pathway. (b) illustrates different parts of the thalamus. VA, VL, VP, LD, and LP refer to the ventral anterior, ventral lateral, ventral posterior, lateral dorsal, and lateral posterior area of the thalamus, respectively. Other sections of thalamus, such as, anterior, medial, pulvinar, lamina and internal medullary lamina are also depicted. In the center, exploded head model is illustrated including cortical and subcortical structures. (c) shows the location of synthetic source at posterior wall of the central sulcus, i.e., Brodmann area 3b that corresponds to the SEP responses. (d) demonstrates the synthetic source (blue) as the main generator for P14/N14 component at medial lemniscus in brainstem and (e) shows an originator in ventral posterolateral (VPL) thalamus. (For interpretation of the references to colour in this figure legend, the reader is referred to the web version of this article.)

in their temporal order of occurrence. The mechanism of detecting the quadrupolar afferent volley in the subcortical structures is explained in (Buchner et al., 1995b); a quadrupole causes a weak field and is, therefore, detectable only at locations with discontinuities in the conductivity distribution, where one of the two dipoles constituting the quadrupole becomes visible. Fig. 2 depicts the different anatomical structures of the brainstem and thalamus to enlighten how the active components correspond to the deeper structures.

### 2.4.1. P14/N14

P14, the positive component at 14 ms, corresponds to a far-field potential and can be detected with ipsilateral centroparietal (CPi) electrode, using a noncephalic reference, normally the contralateral Erbs point (EPc). In (Buchner et al., 1995a), its visibility in the stimulation of the right median nerve has been shown for C3, F3 and P3 electrode of a standard 10–20 electrode cap with average reference. The P14 positive far-field peak is generated at 14 ms latency in the brainstem region, particularly, in the medial lemniscus (Buchner et al., 1995a; Mauguière et al., 1983; Noël et al., 1996). The turning point between P14 and N14 is located at the medulla-pontine junction. Thus, the location of the P14 peak is considered to be above the cuneate nucleus (Passmore et al., 2014; Urasaki et al., 1990) which travels to the ventral posterolateral part of the thalamus (Mauguière et al., 1983).

### 2.4.2. P16/N16

The far-field potential for the P16/N16 component is located either at the sub-thalamic region or it constitutes a thalamo-cortical radiation (Buchner et al., 1995b; Tsuji et al., 1984). The P16 component revealed subcortical activity in the ventral thalamus which was maintained in patients with a lesion in Buchner et al. (1995b). Furthermore, a study by Hsieh et al. (1995) depicted that a negative peak, N16, originates

from the cuneate nucleus. In Tsuji et al. (1984), N16 is suggested to reflect the subcortical activity onto the fronto-central areas.

### 2.4.3. P18/N18

At 18 ms, the far-field activity is a relatively widespread bilateral distribution and involved with multiple generators from the brainstem (Mauguière et al., 1983; Noël et al., 1996) to the upper midbrain and the thalamus, where the negative peak, N18, is detectable (Mauguière and Desmedt, 1989; Nuwer, 1998; Passmore et al., 2014). In Urasaki et al. (1990), the N18 peak is suggested to be generated between the upper pons and midbrain, excluding the thalamus as an active area. However, (Noël et al., 1996) recommended that the N18 peak is originated in the lower medulla nuclei and the study by (Sonoo et al., 1992) concluded that the N18 peak is derived from the dorsal column to the cuneate nucleus by the primary afferent depolarization.

### 2.4.4. P20/N20

The P20/N20 component reflects the maximum peak of the primary somatosensory cortex (SI), which is located at the posterior bank of the central sulcus in Brodmann area 3b (Allison et al., 1991; Antonakakis et al., 2019; Buchner et al., 1994; Fuchs et al., 1998) and can be observed from a contralateral centroparietal (CPc) electrode measurement using CPi electrode as a reference (Fried et al., 2014). The visibility of P20/N20 in the F3 electrode of 10–20 system (right median nerve) with average reference has been shown in Buchner et al. (1995a). As a thalamo-cortical projection, thalamus can be active simultaneously as shown, e.g., in Götz et al. (2014).

### 2.4.5. P22/N22

The maximum peak of 22 ms latency is detectable at the crown of either the first precentral (Brodmann area 4) or postcentral (Brodmann

area 1) gyrus corresponding to a radially-oriented source (Allison et al., 1991; Buchner et al., 1994; Fuchs et al., 1998). Correspondingly, thalamus was found to be active when the maximum amplitude was detected for the P22/N22 component (Papadelis et al., 2011). In the subcortical structure, the maximum amplitude for the P22/N22 component was found to be located at the thalamus (Haueisen et al., 2007).

### 2.4.6. P30/N30

The peak 30 ms post-stimulus builds a network between cortical and subcortical structures including the basal ganglia, thalamus, premotor areas, and primary somatosensory cortex, and is employed as a marker for sensorimotor processing (Passmore et al., 2014). Namely, it links the motor, pre-motor and pre-frontal cortex area (Cebolla et al., 2011; Chéron et al., 1994; Passmore et al., 2014). Moreover, Cebolla et al. (2011) suggested that the P30/N30 component involves somatosensory activity which is located in Brodmann area 3b (Allison et al., 1991; Buchner et al., 1994) of the primary somatosensory cortex. However, it does not show that maximum activity contributed to this area. Particularly, N30, corresponds to the pre-central (BA4 and BA6) and the pre-frontal (BA9) cortex (Cebolla et al., 2011), in which also deep structures, namely, basal ganglia and ventrolateral thalamus were identified, when N30 was at its maximum peak (Cebolla et al., 2011; Passmore et al., 2014; Pierantozzi et al., 1999; Schell and Strick, 1984).

### 2.5. Subjects and ethical clearance

SEP datasets for this study were obtained for three right-handed healthy adult male subjects (**I**), (**II**) and (**III**), 49, 32 and 27 years old, respectively. The subjects had no history of psychiatric or neurological disorders and had given written informed consent before the experiment. The institutions ethical review board (Ethik Kommission der Ärztekammer Westfalen–Lippe und der WWU) approved all experimental procedures on 02.02.2018 (Ref. No. 2014-156-f-S). The Neurophysiological data and head model (for one subject) are available at the Zenodo portal.[1]

### 2.6. MRI acquisition and SEP data preprocessing

For each head model, MRI dataset was measured by MAGNETOM Prisma scanner 3.0 T (Release D13, Siemens Medical Solutions, Erlangen, Germany) with T1-weighting (T1W) fast gradient-echo pulse sequence using water selective excitation to avoid fat shift (TR/TE/FW = 2300/3.51 ms/8°, inversion prepulse with TI = 1.1 s, cubic voxels of 1 mm edge length) and T2-weighting (T2W) turbo spin echo pulse sequence (TR/TE/FA = 3200/408 ms/90°, cubic voxels, 1 mm edge length).

The SEP measurements were performed by stimulating the median nerve of the right wrist with the subjects lying in a supine position in an electromagnetically shielded room to avoid head movement and cerebrospinal fluid (CSF) effects due to the brain shift in relation to the MRI (Rice et al., 2013). SEP measurements were performed using 80 AgCl sintered ring electrodes (EASYCAP GmbH, Herrsching, Germany) including 74 EEG channels in total (10–10 system) and excluding defective sensors in the pre-processing step.

The electrode positions of the EEG cap were digitized using a Polhemus device (FASTRAK, Polhemus Incorporated, Colchester, Vermont, U.S.A.) before the measurements. Following the guideline of averaging 1000–2000 trials for spinal and subcortical SEPs (Cruccu et al., 2008), a total number of 1200 stimuli were obtained during a 9 min measurement session. The monophasic electrical pulse duration was 0.5 ms, and to determine the magnitude, the stimulus strength was increased until thumb twitching was observed.

In the pre-processing stage, the measurement was divided into equally large segments of 300 ms, subdivided into 100 ms pre-stimulus,

stimulus and 200 ms post-stimulus sub-intervals. The inter-stimulus interval varied randomly and uniformly between 350 and 450 ms to avoid habituation. The frequency range from 30 to 600 Hz was investigated as the best possible approximation of the 30 to 3000 Hz reference interval for SEPs (Aminoff, 2012) incorporating the Nyquist criterion with respect to the applied 1200 Hz sampling rate. A notch filter was applied to eliminate the interference caused by the 50 Hz power line frequency and by the 60 Hz of the monitor (where the subjects watched a video during the measurement to increase their attention), including the harmonics.

The responses measured for the different stimuli were averaged to produce the SEP data, the amplitude of which was normalized to one. The FieldTrip software was applied to first visually reject the bad channels and then to reduce the non-cerebral activity based on a threshold-based procedure. This was followed by visual inspection of the candidate bad trials in each modality.

The time points for the SEP components were chosen by first detecting the P14/N14 and P20/N20 peaks from the averaged measurement data, as these have shown to be clearly detectable based non-invasive electrode measurements, as described above and demonstrated in Buchner et al. (1995a); Fried and Legatt (2012); Fried et al. (2014); Götz et al. (2014); Haueisen et al. (2007). This process was to reduce any potential inter-individual latency differences due to, e.g., the subjects' different arm lengths (62, 60, 62 cm for (**I**), (**II**) and (**III**), respectively), room temperature (here the same constant for each subject) and stimulus amplitude (here twice the motor threshold) Stühr (2005). The difference between the observed mean latencies of P14/N14 and P20/N20 has been suggested to be 6 ms (with standard deviation of < 1 ms) Connemann et al. (1999) which was observed to be the difference also with the subjects of this study. The other components were fixed based on their mean difference to the observed P14/N14 peak, which for P16/N16, P18/N18, P22/N22, and P30/N30 has been found to be 2, 4, 6, and 16 ms (with standard deviation of < 1 ms) greater than the latency of P14/N14 with smaller than 1 ms discrepancies Connemann et al. (1999); Hoshiyama and Kakigi (2001); Hsieh et al. (1995).

The relationship between the average referenced data and the topography is illustrated in Fig. 3. It shows the SEP components' traces at different latencies and the corresponding topography for subject (**I**). To show the correspondence of these data and the findings of Buchner et al. (1995a) for P14/N14, P18/N18, P20/N20, and P22/N22, see Figure 8 therein, and Buchner et al. (1994) for P30/N30, the latencies chosen have been overlaid with the curves of electrodes F3, C3 and P3.

### 2.7. Numerical implementation with Zeffiro interface

The forward and inverse solvers applied in this study were implemented in Matlab (The MathWorks Inc.) as a part of the *Zeffiro Interface* (ZI) (He et al., 2019) code package which is openly available in GitHub.[2] ZI is a tool enabling finite element (FE) based forward and inverse computations in electromagnetic brain applications. The forward approach of ZI together with the basic version of the IAS inversion approach have been validated numerically in Calvetti et al. (2009); Miinalainen et al. (2019); Pursiainen (2012). ZI generates a uniform tetrahedral finite element mesh. Each source distribution is obtained by picking a randomly (uniformly) permuted set of tetrahedron centers in the brain compartment. Due to the uniform mesh structure, this strategy leads to an evenly distributed set of source points.

### 2.8. Finite element mesh

The FE mesh was generated based on T1-weighted and T2-weighted MRI sequences measured by a 3T MRI scanner. A six-layer tissue com-
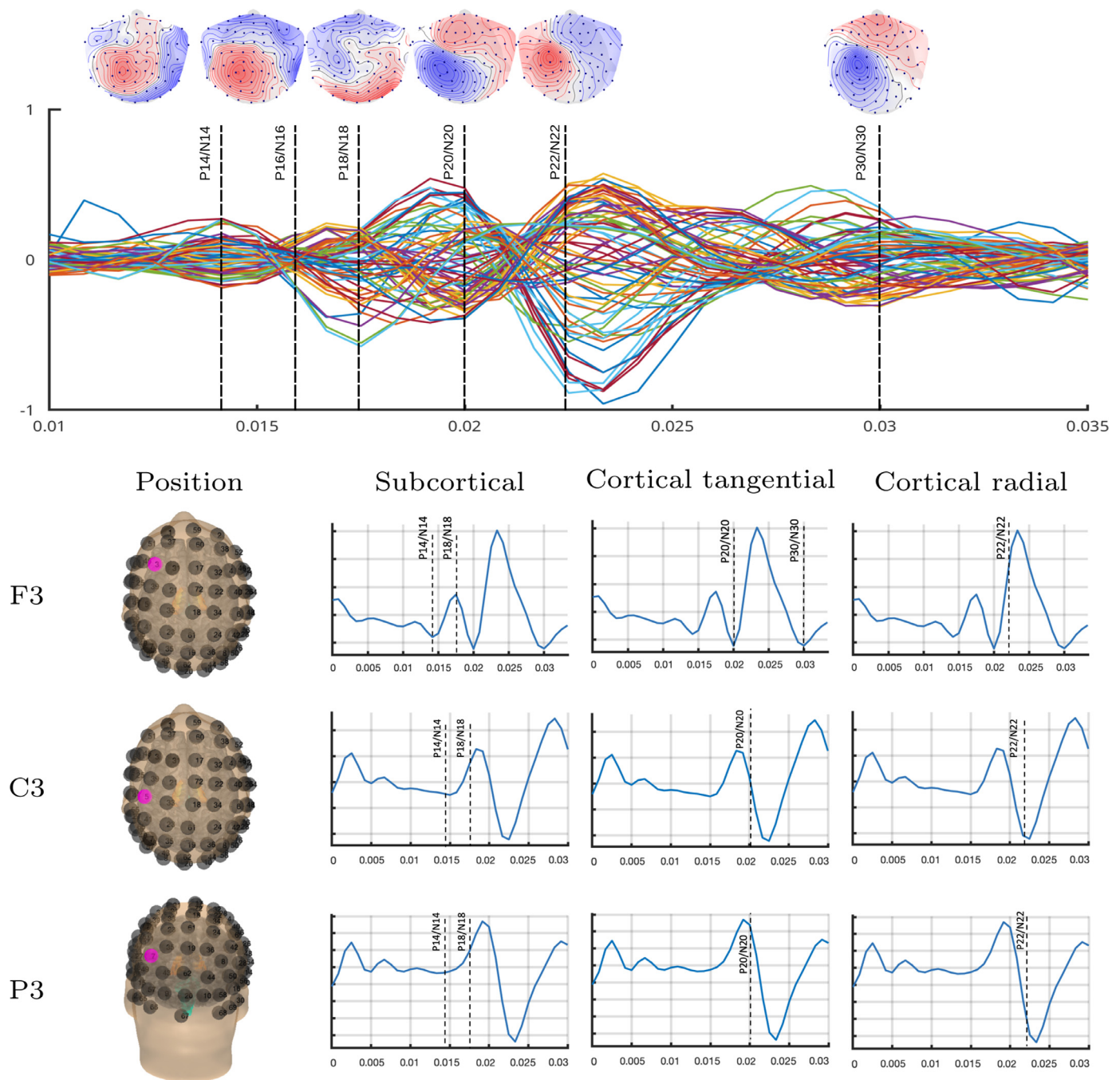
---

**Fig. 3. 1st row:** Butterfly visualization of the SEP components' traces and the corresponding topographies for different latencies as obtained for Subject (I). **2nd–4th row:** To show the correspondence of these data and the findings of Buchner et al. (1995a) for P14/N14, P18/N18, P20/N20, and P22/N22, see Figure 8 therein, and Buchner et al. (1994) for P30/N30, the latencies chosen have been overlaid with the curves of electrodes F3, C3 and P3. The components determined by mainly subcortical, cortical tangential and cortical radial originators are shown in the vertical columns from left to right, respectively. Likewise in Buchner et al. (1995a, 1994), F3 corresponds to P14/N14, P18/N18, P20/N20 and P30/N30, C3 to P18/N18 and P22/N22, and P3 to P22/N22.

partment conductivity model was used: skin, scalp (0.33 S/m), skull (0.0064 S/m), cerebrospinal fluid (CSF) (1.79 S/m), white matter (0.14 S/m) and gray matter (0.33 S/m) (Dannhauer et al., 2011). The different tissue compartments were reconstructed by the FreeSurfer[3] software suite. The subcortical structures were extracted based on FreeSurfer's Aseg atlas. The conductivity of these structures was coupled to that of the cerebral cortex, i.e., 0.33 S/m similar to, e.g., Shahid et al. (2014). The eventual FE mesh was obtained by importing the resulting surface

segmentation to ZI, where a 1 mm resolution FE mesh with 28 M tetrahedra and 4 M nodes was generated per single head model.

*2.9. RAMUS Inversion*

The inverse RAMUS technique was applied for 5 decomposition levels from the coarsest to the finest level. The sparsity factor, that is, in RAMUS, the ratio between source counts for two subsequent resolution levels, was set to be 10, the total number of decompositions was 500, and that of the source positions was 100,000. Following from the orien-

tation of the cortical pyramidal cells (Creutzfeldt et al., 1962; Schmidt and Thews, 1990), the cortical responses were associated with the direction of the cortex surface *normal*. The orientation of the activity was not constrained in the subcortical nuclei, where the neurons do not have a distinct orientation with respect to the surface (Attal et al., 2012).

The shape and scaling parameters of the hyperprior were set to $\beta = 3$ and $\theta_0 = 1\text{E-}8$. Of these, the scale parameter is the governing one. It coincides with the value range applied in Rezaei et al. (2020b). The shape parameter affects the tail-length of the hyperprior and, thereby, the magnitude of the actual source currents (outliers) in comparison to the fluctuations due to the noise effects. A justification for the present choice and approach to choose $\beta$ and $\theta_0$ can be found in Rezaei et al. (2020a) in which a model for selecting hyperprior parameters in the case of single but variable source space resolution was developed via numerical simulations and also the present SEP datasets. In this model, the scale parameter is of the form $\theta_0 = \theta_0^{(total)}/N$ following from the requirement that the hyperprior variance per a volume unit is maintained constant despite the varying source space density. In RAMUS, this model is applied considering the coarsest source space resolution, since it is the first resolution level in the iterative reconstruction process, i.e., here $\theta_0^{(total)} = 1E - 7$ and $N = 10$.

The scale parameter choice can be also motivated via the *a priori* expected realization (noise level) of the unknown, which is given by the expectation of the hyperprior, i.e., $\sqrt{\theta_0/(\beta - 1)} = \sqrt{1\text{E-}8/2}$ (Section 2.1), which is roughly 3E-2·2E-9·1E6, where 3E-2 is the 3% noise standard deviation, 2E-9 Am (3 nAm) a coarse estimate for the smallest *a priori* detectable neural source amplitude, and 1E6 scaling factor in micro units, as the measurement units are in microvolts and the lead field matrix is in SI-units. With the tail set by the shape parameter, the actual currents will have approximately 1E-9 times the hyperprior probability of the noise fluctuations, which we assume to appropriately ensure, on one hand, that the noise effects in the reconstruction will be minimal and, on the other hand, the probability of detecting an actual source will be sufficiently large compared to the numerical accuracy of the solver, i.e., machine epsilon which with the current 64-bit binary floating point accuracy may be assumed to be less than 5E-16.

### 2.10. Alternative source localization techniques

Alternative UNGB, sLORETA, and MNE reconstructions were obtained for the highest-resolution source space. UNGB and sLORETA were selected as they are depth-weighted techniques, thereby allowing for more accurate reconstruction of deeper sources than the classical MNE, which here is considered as an alternative optimization technique to the IAS applied in RAMUS, as it constitutes the first step of the IAS iteration.

The level of regularization for sLORETA and MNE was obtained from the scale parameter which can be associated with the variance of a Gaussian prior as shown in Rezaei et al. (2020a). Thereby, the MNE regularization parameter is of the form $\theta_0^{(total)}/(\sigma^2 N)$ as found in Rezaei et al. (2020a). The current parameter choice is within 10 dB range from the default MNE regularization used, for example, in the Brainstorm software Tadel et al. (2011); Tutorial 22: Source estimation (2020). In UNGB, to obtain the best possible performance for the different SEP latencies, the data covariance matrix was calculated separately for each latency using the measurement dataset of that latency Van Veen et al. (1997). The standard regularized form $\mathbf{C} + \lambda\mathbf{I}$, where $\lambda = 0.05$ as, e.g., in Jaiswal et al. (2020), was applied.

We also tested the performance of MNE-RAMUS, i.e., RAMUS with MNE as the optimization technique instead of IAS. More generally, MNE can be interpreted as the MAP estimate corresponding to a nonconditional Gaussian prior model, whose prior variance is fixed to the initial stage of the IAS MAP estimation process (Calvetti et al., 2009). Moreover, to find the effect of randomization and averaging, we performed a test with single-decomposition RAMUS, i.e., RAMUS recon-

**Table 1**

The computing time for each reconstruction method obtained using an office workstation with 3.70 GHz 10-core CPU (FP32 performance 1,504.0 GFLOPS), 128 GB RAM, and GPU (FP32 performance 7.119 TFLOPS) with 8 GB of GPU RAM is presented in seconds. For RAMUS, the reconstruction time was evaluated for 500, 100, and 10 decompositions.

| Computing time | |
|---|---|
| Method | Time (seconds) |
| RAMUS (500 dec) | 256.0 s |
| RAMUS (100 dec) | 50.4 s |
| RAMUS (10 dec) | 5.4 s |
| sLORETA | 0.7 s |
| Beamformer | 35.5 s |
| MNE | 0.28 s |
| MNE-RAMUS | 63.9 s |

struction obtained by a single multiresolution decomposition without averaging.

### 2.11. Experiments

The primary current distribution corresponding to P14/N14, P16/N16, P18/N18, P20/N20, P22/N22, and P30/N30 component was reconstructed using RAMUS, UNGB and sLORETA and the data of subjects (**I**), (**II**), and (**III**). To complement these experiments, we conducted numerical tests utilizing the head model of the subject (**I**) and synthetic dipolar sources for modelling the P14/N14 and P20/N20 components (Fig. 2) and comparing the obtained reconstructions with RAMUS, MNE and MNE-RAMUS. Additionally, the following numerical tests (Fig. A.6 Appendix) were performed: (a) a source configuration with numerically modelled auditory sources in the left hemisphere was examined as a complementary numerical source setting for simultaneous subcortical vs. cortical source localization; (b) an extended source $\mathbf{x}^{(e)}$ was created via projecting and backprojecting a dipolar source $\mathbf{x}^{(d)}$ as given by $\mathbf{x}^{(e)} = \mathbf{L}^T\mathbf{L}\mathbf{x}^{(d)}$; (c) a single source with location corresponding to (i) postcentral gyrus, (ii) posterior bank of the central sulcus, and (iii) posterior part of the upper brainstem was reconstructed using RAMUS with 5 and 3 resolution levels, and comparing the results with a single-level reconstruction obtained with the coarsest level of 5 and 3 and with the highest resolution in each case; (d) maps of the spatial mean error and standard deviation (Hauk et al., 2011) were evaluated for RAMUS, UNGB and sLORETA reconstructions to approximate the mean localization error and dispersion in reconstructing a single dipole. Each measure was obtained in a 60 mm diameter sphere centered at the dipole location. In all numerical tests, zero-mean Gaussian white noise with standard deviation of 3% with respect to the maximum data amplitude was added to the noiseless simulated data.

### 3. Results

The results obtained with RAMUS and the alternative techniques UNGB, sLORETA, MNE, and MNE-RAMUS are shown on (1) a high-resolution folded cortex surface with 600.000 triangular surface elements, (2) a downsampled inflated cortex with 100,000 triangular surface elements and (3) a subcortical structure including left and right thalamus and brainstem. The maximum amplitude of each reconstruction is normalized to one. In the inflation process, downsampling was applied to enhance the regularity of the surface geometry and the quality of the visualization. The computing time for each reconstruction, i.e., RAMUS (5 levels, 500, 100, and 10 decompositions), sLORETA, UNGB, MNE, and MNE-RAMUS is presented in Table 1.

### 3.1. Reconstruction of SEP components

The reconstructions of the measured and numerically simulated SEP components can be found in Figs. 4 and 5. Fig. 4 visualizes the reconstructions obtained for the P14/N14, P16/N16, P18/N18, P20/N20, P22/N22, and P30/N30 components with respect to both cortical and deep activity for subjects (I)–(III). The effect of the RAMUS technique is demonstrated in Fig. 5 via complementary reconstructions. We first consider the results obtained for the subject (I), whose dataset was used as a reference in selecting the parameters of the reconstruction process. Then, the comparisons to the subjects (II) and (III) as well as to the complementary results are presented in Figs. 4 and 5. Further complementary reconstructions were obtained for the numerically simulated auditory sources that can be found in Appendix (Fig. A.6(a)).

### 3.2. Subject (I)

The deep P14/N14 component in subject (I) (Fig. 4) is reconstructed in the areas from the brainstem to the midbrain. In other words, the subcortical activity reflects the afferent volley traveling from the medial lemniscus to the thalamus. The activity was also weakly projected to the cortical areas, notably to the parietal lobe. This weak activity might occur due to the ongoing processing of the preceding trial, even when trying to reduce phase-locking by means of the randomization of the inter-stimulus interval when the stimulation is still going on with later trials.

The deep activity of the P16/N16 component is here found in the lower part of the brainstem, particularly in the cuneate nucleus, and it is also distributed over the anterior and ventral thalamus. This projects slightly onto the cortical surface mainly in the frontal part, which we interpret to be the result of the above-mentioned uncertainty (noise) effects of the measurement and stimulation process.

The activity for the P18/N18 component was found to be widely distributed over the brainstem. It is maximized in the lower part of the medulla, dorsal column, decreasing towards the upper pons and midbrain. As can be observed from the results, the thalamus is slightly active on the ventral posterolateral (VPL) part. The cortical projection reflects the activity from the occipital lobe to the parietal region, which we interpret as a potential consequence of the measurement and stimulation uncertainties, e.g., inter-stimulus cortical activity remainder.

The cortical activity for P20/N20 component is located at the primary somatosensory cortex (SI), cytoarchitectonic area 3b at the posterior wall of the central sulcus. The corresponding deep activity was found to be widespread, extending from the medulla to the thalamus with its maximum in the midbrain and the ventrolateral region of the left thalamus.

The cortical part of the P22/N22 reconstruction was concentrated on the parietal lobe, especially the postcentral gyrus. The deep activity was maximized in the left ventral thalamus with some contribution to the medulla and midbrain.

The P30/N30 amplitude was found to be visible in the post-central cortex and frontal lobe (BA4, BA6, and BA9). In the former, both the sulcus (SI) and the gyrus were activated, whereas, in the latter, particularly BA4 and BA6, the activity was mainly sulcal. The subcortical amplitude was found to be concentrated on the ventrolateral part of the left thalamus, and also from the upper part of the pons to the midbrain.

### 3.3. Comparison to subjects (II) and (III)

Comparing the experimental results (Fig. 4) obtained in subject (I) to the cases of (II) and (III), one can observe that the cortical (sulcal and gyral) and subcortical (thalamic and sub-thalamic) activity components are essentially similarly distinguished in each case with the following differences.

In the case of (II), the activity observed for P14/N14 and P16/N16 is overall more focused on sub-thalamic structures than in (I). The tha-

lamic activity observed for the subject (I) corresponding to P16/N16 is absent. P18/N18 includes an early cortical projection (red) due to the remaining phase-locked activity of the preceding trial. In the case of subject (III), P14/N14 and P16/N16 involve an occipital projection which is absent in (I) and (II). Akin to (II), P18/N18 involves an early cortical projection. Subject (I) reveals mainly only contralateral dipolar activity for P20/N20, while subjects (II) and (III) show slight ipsilateral activation with topographies that are not only contralateral, but also ipsilateral dipolar activation which might be due to remaining and possibly also bi-lateral phase-locked activity to the preceding trial. In the case of P22/N22, the thalamic activity is suppressed compared to (I).

In the case of subject (III) the reconstructed cortical activity for the P30/N30 emerged to be more widespread and includes a stronger frontal contribution compared to (I) or (II), while the post-central gyrus and 3b area more strongly reconstructed for the subject (II). Furthermore, according to the topography for each subject (Fig. 4), the P30/N30 component for subject (I) has opposite polarity compared to subjects (II) and (III).

### 3.4. Comparison to alternative reconstruction techniques

In the reconstructions obtained with unit-noise gain beamformer (UNGB) and sLORETA (Fig. 4) for subject I, the reconstructed activity is concentrated on deep structures between 14 to 18 ms, particularly, at brainstem and medial lemniscus while no activity is detected on the cortical surface. At 14 ms, the maximal current is detected at the pons with both UNGB and sLORETA. Akin to RAMUS, at 16 and 18 ms, the activity is maximized close to the cuneate nucleus, the lower part of the medulla, with sLORETA but not with UNGB. Compared to RAMUS, the components from 20 to 30 ms with simultaneous cortical and subcortical activity have a less distinct cortical projection when reconstructed with UNGB and sLORETA. For the sulcal component of P20/N20 this is the case only with UNGB, and for the gyral P22/N22 with both UNGB and sLORETA. At 30 ms, both UNGB and sLORETA show simultaneous cortical and subcortical activity, which has a weaker gyral contribution compared to the RAMUS reconstruction. Similar to RAMUS, the UNGB and sLORETA reconstructions obtained with subjects (II) and (III) are overall in line with the case of subject (I). The early cortical projection obtained with RAMUS at 18 ms was observed also with UNGB and sLORETA. In the case of UNGB, it is more suppressed than with sLORETA, which is clearly due to the generally less distinct cortical component yielded by UNGB. Numerically simulated maps of the localization accuracy and dispersion of RAMUS, UNGB and sLORETA can be found in Appendix (Fig. A.6(d)).

### 3.5. Complementary results with synthetic data

Reconstructions of the synthetic P14/N14 and P20/N20 components are presented in Fig. 5. In addition to RAMUS, we applied standard (single-resolution) MNE (Hämäläinen and Ilmoniemi, 1994) method and MNE-RAMUS for multiresolution levels to show and compare the effect of RAMUS on the reconstructed activity.

For P14/N14 component (a), the results obtained with RAMUS are consistent with the source reconstruction on the real dataset in Fig. 4 at 14 ms for component P14/N14, as the activity mainly stems from the medial lemniscus in brainstem whereas cortical activity is diminished. MNE reveals no strong activity for either the cortex or subcortical region. In contrast, MNE-RAMUS shows the P14/N14 generator reconstructed for the medial lemniscus.

RAMUS for the P20/N20 component (b) demonstrates the focal cortical activity at Brodmann area 3b and simultaneous deep activity at the ipsilateral VPL thalamus which is in line with the reconstructions obtained with the real dataset in Fig. 4 at 20 ms. MNE depicts the reconstructed superficial activity while the deep activity in the VPL thalamus is not very intense compared to that obtained with the RAMUS tech-
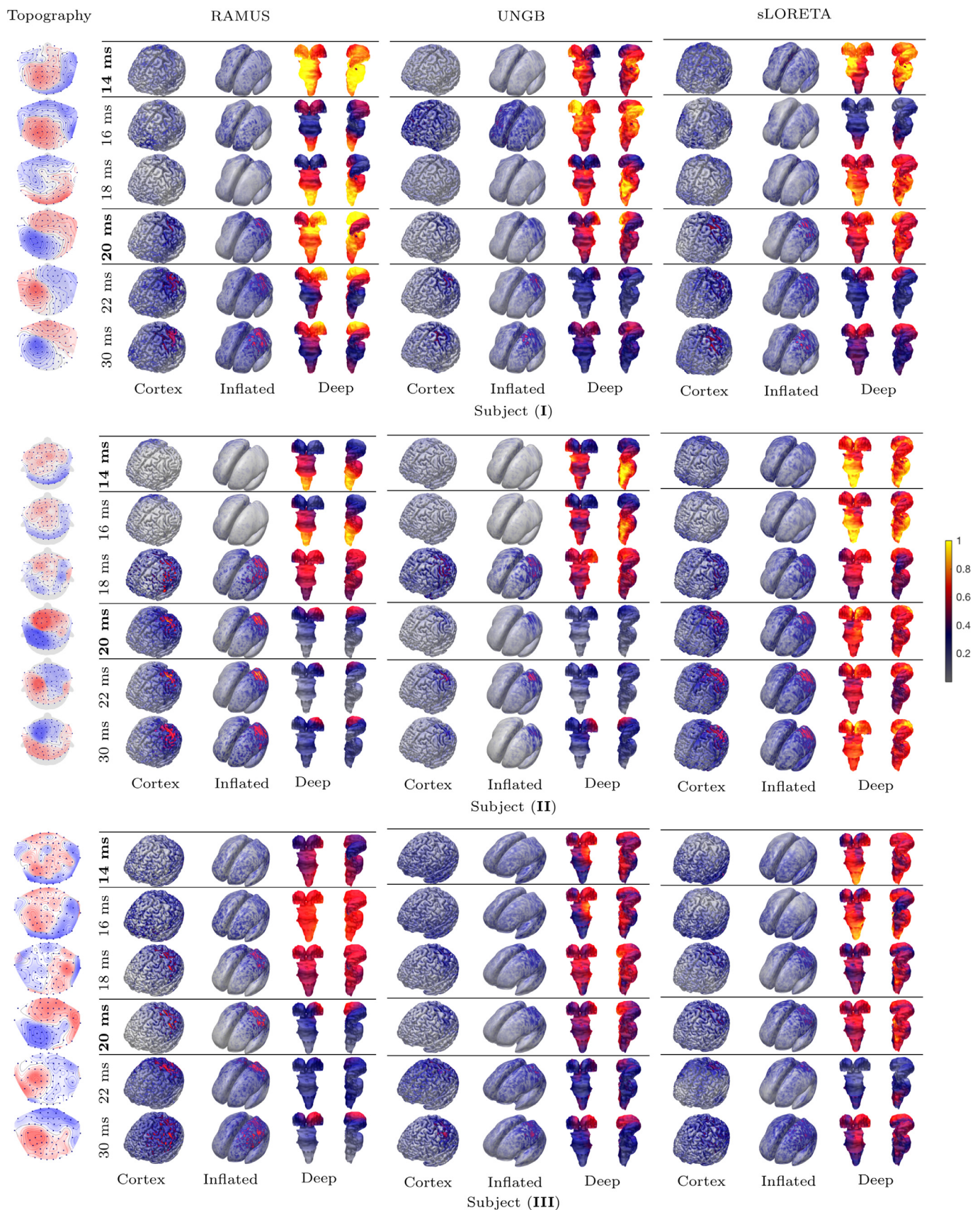
**Fig. 4.** The reconstructions (RAMUS, UNGB and sLORETA) and topographical plots for the 14–30 ms post-stimulus peaks P14/N14, P16/N16, P18/N18, P20/N20, P22/N22, and P30/N30 obtained for subjects (**I**)–(**III**). Horizontal lines highlight the components P14/N14 and P20/N20, i.e., the first subcortical component and the first component involving a known SEP cortical response, respectively. In each visualization, a frontal view of the folded cortex and the inflated surface next to that is shown to demonstrate the cortical activity distribution. The frontal and lateral views of the subcortical reconstructions are also illustrated. The reconstructions are normalized to 1 with respect to the maximum amplitude of the reconstructed activity.
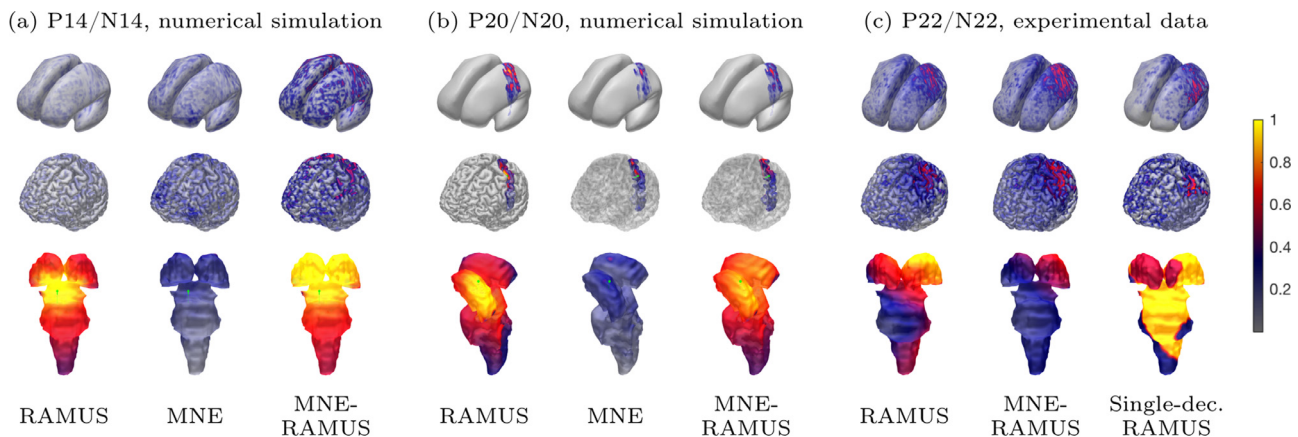
(a) P14/N14, numerical simulation    (b) P20/N20, numerical simulation    (c) P22/N22, experimental data



RAMUS | MNE | MNE-RAMUS    RAMUS | MNE | MNE-RAMUS    RAMUS | MNE-RAMUS | Single-dec. RAMUS

**Fig. 5.** Complementary results obtained using the head model of subject (**I**), visualizing the activity reconstructed with synthetic sources (shown in green with respect to the source locations demonstrated in Fig. 2 (c) and (d)) for P14/N14, and P20/N20, and the reconstructions obtained with the experimental data of the P22/N22 component measured in subject (**I**). For P14/N14, and P20/N20, the following three reconstructions are shown: RAMUS, MNE, and MNE-RAMUS; the last one is a technique in which RAMUS is applied using MNE instead of the IAS as the optimization algorithm. Single-decomposition RAMUS (Single-dec. RAMUS), i.e., RAMUS without averaging, was applied in the case of P22/N22. The reconstructions are normalized to 1 with respect to the maximum amplitude of the reconstructed activity. (For interpretation of the references to colour in this figure legend, the reader is referred to the web version of this article.)

nique. MNE-RAMUS shows the cortical activity as well as distributed deep activity in thalamic nuclei for P20/N20 component.

### 3.6. Complementary results with experimental data

The P22/N22 component is involving both extremely superficial (gyral) and deep activity and was investigated in complementary source localization tests which are performed for subject (**I**). P22/N22 was selected for these tests as it was generally the most sensitive SEP component with respect to the parameter changes. Subfigure (c) of Fig. 5 demonstrates the effects of the resolution, multiresolution decomposition, and randomization observed in the tests. MNE-RAMUS found both deep and superficial activity, the former one of these being, however, less pronounced than in the case of RAMUS. When multiple resolution levels were used without randomization or averaging, i.e. single-decomposition RAMUS was applied, the cortical activity was found to be reconstructed on the crown of the gyrus and the deep activity was detected simultaneously, however, with a considerably coarser pattern than with multiple decompositions.

## 4. Discussion

### 4.1. Our observations

The recent studies Pizzo et al. (2019); Seeber et al. (2019) have suggested that the scalp measurements can be sufficient to distinguish subcortical brain activity. These findings concern a high-definition electrode configuration and frequency filtering, respectively. Here, in addition to the deep activity, we consider the Brodmann area 3b activity for P20/N20, radial and focally lateral activity for P22/N22 (Papadelis et al., 2011), and extended activity for Brodmann area 3b for P30/N30 component (Cebolla et al., 2011). Our observations compared to original patterns referring to the existing literature can be found summarized in Table 2.

Based on the presented results, we consider RAMUS (Rezaei et al., 2020b) to be a promising technique to detect activity in both cortical and subcortical structures potentially improving the capabilities of the underlying IAS technique. The results were obtained for the healthy adult subjects (**I**)–(**III**) suggest that RAMUS detected the early 14–30 ms cortical and subcortical responses to median nerve SEP appropriately with respect to the physiological literature reviewed in Section 2.4. Furthermore, the reconstructions obtained for different subjects have an ap-

propriate mutual similarity with some differences which might be due to remaining noise, remaining phase-locking to the preceding trial and discrepancies in signal processing. This might affect especially the subcortical components which are sensitive to noise, and to subject-wise variation, e.g., in the thalamo-cortical radiation (Buchner et al., 1995b), which is a possible cause of the intersubject differences observed in the thalamic activity at 16 ms and the early cortical projection detected at 18 ms post-stimulus in (**II**) and (**III**). Besides the results obtained with the experimental data, numerical simulations suggest that we can find parallel results with simulated P14/N14 and P20/N20 components. An additional source configuration including a dipole in the supratemporal gyrus of the left hemisphere and in the posterior part of the upper brainstem was included to demonstrate the functionality of the RAMUS technique for finding a reconstruction in another potential setting involving both superficial and deep activity.

We used the frequency range of 30–600 Hz, a subinterval of the widely applied 30–3000 Hz, where the latter follows the guideline by Aminoff (2012). The upper limit of the range applied was the highest possible to follow the Nyquist criterion, with respect to the 1200 Hz data sampling frequency. Having high enough frequencies presented in the data was found to be necessary, in particular, for distinguishing subcortical activity. To the best of our knowledge, we provide the first results in the context of inverse modelling to reconstruct not only the subcortical activity but also analyzing its connection to the cortex simultaneously for different consecutive time points. Following this, no other constraints in addition to those concerning the physiology of the active tissue, which highlights the potential applicability of our approach in the analysis of somatosensory networks, i.e., the brain areas involving SEPs as a response to a stimulus, as well as their function and connectivity.

Our results suggest that, in RAMUS, both multiple resolution levels and randomized decompositions are significant features. The 5 resolution levels and 500 decompositions utilized in the reconstruction process were considered to be sufficient for generating a robust and focal enough estimate for the cortical and subcortical activity. That is, the obtained estimate is principally the same between different inversion runs. Using a lower number of decompositions, e.g., 100, was found to lead to some amount of random fluctuations. With the current set of multiple resolutions, we could reconstruct sources with different depths, contrary to our tests with a single-resolution. Moreover, we showed that to reconstruct simultaneous gyral and thalamic activity appropriately, it is advantageous to apply both multiple resolution levels and multi-

**Table 2**

A summary of our observations w.r.t. the activity reconstructed via RAMUS (Fig. 4) and patterns reported in the literature.

| Peak | Observation | Literature |
|------|-------------|------------|
| **P14/ N14** | Activity is mainly restricted to the subcortical part. Minor cortical fluctuations were observed due to remaining phase-locked activity of the preceding trial. Maximum activity matches roughly with the medial lemniscus pathway. Intersubject variations inside the subcortical structure concern mainly the area of the thalamus. | Subcortical generator for P14 positive peak is distinguished above the cuneate nucleus (Urasaki et al., 1990) and in brainstem region, especially, medial lemniscus (Noël et al., 1996) to VPL part of the thalamus (Mauguière et al., 1983). The turning point between P14 and N14 is located at the medulla-pontine junction. |
| P16/ N16 | Activity is mainly restricted to subcortical region. Maximum in thalamus observed in (**I**) is absent in (**II**) and (**III**). | P16/N16 subcortical activity occurs mainly in the sub-thalamic region. The generator for this component stems from cuneate nucleus and VPL thalamus (Buchner et al., 1995b; Hsieh et al., 1995). |
| P18/ N18 | Activity is mainly limited to the subcortical area in (**I**), while (**II**) and (**III**) show a cortical projection. | This component has multiple generators in the brainstem (Mauguière et al., 1983; Noël et al., 1996). The subcortical activity originates from lower medulla (Noël et al., 1996) to upper pons and midbrain (Urasaki et al., 1990). Some studies pointed out this component does not include any activity in thalamus area (Urasaki et al., 1990). |
| **P20/ N20** | The cortical activity is maximal in the Brodmann area 3b in the central sulcus of contralateral hemisphere and the subcortical activity in the VPL region of the left thalamus and, in subject (**I**), also in the midbrain. | P20/N20 component demonstrates the maximum peak at cortex at the posterior bank of central sulcus, i.e., Brodmann area 3b (Allison et al., 1991; Buchner et al., 1995a) and corresponding subcortical activity in the thalamus. |
| P22/ N22 | Contralateral Brodmann area 1 in the left postcentral gyrus and the ventral thalamus were found to be activated. Subjects (**II**) and (**III**) have a suppressed subcortical component w.r.t. (**I**). | Maximum cortical activity for P22/N22 is in the crown of either the precentral (Brodmann area 4) or postcentral (Brodmann area 1) gyrus (Buchner et al., 1994) and the deep activity in the thalamus (Haueisen et al., 2007; Papadelis et al., 2011). |
| P30/ N30 | The posterior wall of the central sulcus, i.e., Brodmann area 3b corresponding to the primary somatosensory cortex (SI) is reconstructed. The crown of gyral component in the contralateral Brodmann area 1 in the postcentral gyrus and the left ventrolateral thalamus were found to be active. The activity involves a frontal contribution and is spread over a larger area than in the case of P22/N22, especially for subject (**III**). | The cortical activity for this component occurs in pre-central (BA4 and BA6) and the pre-frontal (BA9) cortex including BA 3b. The subcortical activity pattern includes deep structures, e.g., basal ganglia and ventrolateral thalamus (Cebolla et al., 2011; Passmore et al., 2014). |

ple decompositions. Namely, on one hand, if only the high resolution is applied, the deep activity will be absent. On the other hand, higher resolution levels are required to reconstruct a cortical activity pattern which matches with the literature knowledge, especially, that concerning the gyral P22/N22 component occurring a few milliseconds after the 20 ms time point (Papadelis et al., 2011). The visualization of the P22/N22 component obtained with the lowest resolution level shows the activity in the deep structures and no maximum peak visible on the gyrus. Compared to the eventual averaged estimate, the structure of the reconstructed activity is coarser, which is obvious, especially regarding the subcortical structures. These results indicate that randomized multiresolution decompositions in the context of HBM can be vital to visualize both deep and cortical activities to detect the correct pattern for various SEP components.

### 4.2. Parameter selection

The choice of the scale parameter was found to be essential for source localization, which here is extended from the extremely superficial (gyral) area to the deepest one, i.e., the thalamus and brainstem which spatially cover the center part of the volume conductor model. With the shape and scale parameter $\beta = 3$ and $\theta_0 = 1E - 8$ of which the former has been applied in Calvetti et al. (2009) and the latter is in the range suggested in Rezaei et al. (2020a,b), we could reconstruct the investigated network of the SEP components independently of the location of the corresponding activity. The present combination of $\beta$ and $\theta_0$ can be motivated (Section 2.9) by fitting the expectation of the hyperprior to that of the noise and setting the weight of its tail to minimize any noise effects while maintaining the numerical accuracy of the solver. For comparison, with a lower value of $\theta_0$, the balance was found to be overly deep and leading to a missing gyral component, while with a larger one, the deep activity was not detected. With this regard the gyral component was found to be more sensitive compared to the sulcal one, which was the most robust of the investigated components with respect to the selection of $\theta_0$. The tendency of the HBM to produce deeper reconstructions along with a decreasing scale parameter has been shown in He et al. (2019). Due to the different capabilities of the low and high resolution levels, it is obvious that the optimal choice for $\theta_0$ might de-

pend also on the applied resolution. We assume that a coarse source space favors a larger $\theta_0$ than a finer one, since the source intensity is distributed over fewer sources, meaning that the expected value per a source is higher. Supporting this notion, a smaller value was found to yield an appropriate overall performance in He et al. (2019), where a single resolution level was used.

### 4.3. Different component reconstructions

Concerning the activity occurring at 14–18 ms, our reconstructions are mainly subcortical with a minor cortical projection as a consequence of the preceding trial, which might overlay to the detected subcortical activity of the latter trials. For the P14/N14 component, the results are in agreement with the existing literature (Buchner et al., 1995a; Mauguière et al., 1983; Noël et al., 1996) suggesting that P14/N14 originates in the brainstem area, especially, in medial lemniscus extending to the thalamus (Mauguière et al., 1983; Tsuji et al., 1984). Akin to our findings, P16/N16 component has been associated with activity in ventrolateral thalamus (Götz et al., 2014) and also in cuneate nucleus (Hsieh et al., 1995). The activity for the P18/N18 component was found to be more broadly distributed which is in accordance with Sonoo et al. (1992); Urasaki et al. (1990) referring to the widespread bilateral propagation due to the generators in the medulla, cuneate nucleus of the dorsal column to the upper pons and midbrain (Sonoo et al., 1992; Urasaki et al., 1990). Component P20/N20 reveals the first post-stimulus cortical activity localized the maximum peak on the sulcal wall with tangential orientation in the primary somatosensory cortex (SI), Brodmann area 3b (Allison et al., 1991; Buchner et al., 1995a; 1994), and thalamus was deemed to have the maximum amplitude for the deep structure activity (Götz et al., 2014; Haueisen et al., 2007). The P22/N22 appears only a few milliseconds after the P20/N20 as also discussed by (Papadelis et al., 2011) and was attributed to the crown of the postcentral gyrus similar to (Buchner et al., 1996), with more radial orientation than the P20/N20 generator, while the deep portion was maximal in the ventrolateral thalamus. At 30 ms latency, subcortical activity mainly involved the ventrolateral thalamus (Passmore et al., 2014), and the cortical response included the pre-central (BA4 and BA6) and pre-frontal (BA9) areas. Moreover, the cortical projection result is in agreement

with (Cebolla et al., 2011) including the somatosensory Brodmann area 3b (Allison et al., 1991).

### 4.4. Limitations and comparison

While the randomized multiresolution scheme of the RAMUS might be applicable in various applications, it is important to point out that in the context of HBM, it is principally applied to reconstructing focal sources. Herein, the accuracy obtained varies based on the source depth decreasing along with the growing depth and is affected also by the number of sources. The earlier findings Buchner et al. (1995b); Götz et al. (2014); Mauguière et al. (1983); Noël et al. (1996); Urasaki et al. (1990) and also the present results demonstrate that the early subcortical components occuring between 14 and 18 ms poststimulus and can be identified as having only subcortical generators, while the later components $\geq$ 20 ms include a cortical contribution. The subcortical activity, which is detected simultaneously with the cortical one from 20 ms onward, also involves more uncertainty compared to the cortical originators. Comparing the outcome of the RAMUS, sLORETA and UNGB reconstruction techniques with these observations, all approaches localize the subcortical activity at earlier latencies. In particular, the 14 ms activity is concentrated near the upper pons for each technique, which is in line with the literature Mauguière et al. (1983); Noël et al. (1996). RAMUS detects the greatest cortical amplitude, while it is fairly suppressed in the case of UNGB and sLORETA. At 20 ms, the weakest cortical component was obtained with UNGB and subject (**II**). While sLORETA found a more distinct cortical component than UNGB, which led to an overall weaker gyral contribution than RAMUS at 22 ms. RAMUS, on the other hand, found the most pronounced early cortical projections at 18 ms that were observed for subjects (**II**) and (**III**). Since this observation is obtained by each reconstruction technique, it clearly seems that this finding not suggested by the literature can be due to other reasons than the reconstruction process itself. The maps are obtained via numerical localization (Fig. A.6(d)) Hauk et al. (2011) of a single dipole, suggesting further that RAMUS compared to UNGB and sLORETA is an advantageous technique for both cortical and subcortical domains considering the mean localization error, while its dispersion might be somewhat elevated in comparison to UNGB; the dispersion tends to increase as coarser levels are included in the multiresolution decomposition which was also shown numerically (Appendix). The maps, however, do not reveal the exact performance in the case of two simultaneous sources.

Due to the complex structure of the brain and the effect of the source configuration, the accuracy and focality that obtained is clearly application specific and depends also on the implementation of the multiresolution decomposition or the optimization method used in RAMUS, e.g., IAS vs. MNE (Hämäläinen and Ilmoniemi, 1994) as demonstrated by the complementary results of this study. The concept and structure of the multiresolution decomposition (Rezaei et al., 2020b) and randomization applied here might be amendable or extendable, regarding, e.g., the optimal source focality obtained versus its sensitivity to detect sources. This might provide a way to improve the focality of some cortical components, especially P22/N22, which in this study was relatively widespread, potentially partly because of its simultaneous occurrence with thalamic activity and partly due to the current approach of averaging over all resolution levels. In general, RAMUS is found to be potentially an advantageous approach for reconstructing the cortical and simultaneous subcortical activity. However, further investigations would be required to evaluate the performance and comparison of RAMUS with other reconstruction techniques.

### 4.5. Future directions

To generalize our findings, a follow-up research in the direction of investigating more subjects and considering other evoked measurements is envisioned. An evaluation of the effect of stimuli repetition on the detection of the deep activity via RAMUS will be carried out. Important directions include analyzing more general aspects of the somatosensory networks, e.g., the role of the cerebellum in median nerve stimulation (Andersen et al., 2020; Dalal et al., 2013; Hashimoto et al., 2003; Samuelsson et al., 2020; Tesche and Karhu, 1997), and also comparing RAMUS to other methods, such as other resolution variation techniques, multi-dipole localization (Krishnaswamy et al., 2017; Samuelsson et al., 2019; Sommariva and Sorrentino, 2014), and the deeper investigation with the beamformer techniques (Andersen et al., 2020; Hashimoto et al., 2003; Neugebauer et al., 2017; Sekihara et al., 2001). In addition to EEG, the applicability of RAMUS in MEG and E/MEG will be examine. A potential alternative for such a study would be auditory evoked field (AEF) analysis, e.g, ASSRs, where MEG data is commonly used in experiments Hari et al. (1989); Pantev et al. (1996).

### Credit authorship contribution statement

### Acknowledgements

### Appendix A. Complementary results

Fig. A.6 includes additional numerically simulated results which complement our analysis conducted on experimental and numerically simulated SEP data. Case (a) shows that RAMUS finds a focal reconstructed activity on the superior temporal gyrus and correlated intense reconstructed activity at the inferior colliculus for deep structure. MNE retrieved the cortical activity while the subcortical activity disappeared. Following this, MNE-RAMUS did not find as strong subcortical activity as RAMUS.

In (b), an extended area of activation was simulated by projecting and backprojecting a dipolar source in the left frontal lobe (left column) and adding noise to the resulting data. A reconstruction was found via both MNE (center column) and RAMUS (right column). Both reconstructions show extended cortical activity in the vicinity of the maximum source amplitude. The amplitude and spread of the reconstructed distribution is slightly greater in the case of RAMUS.
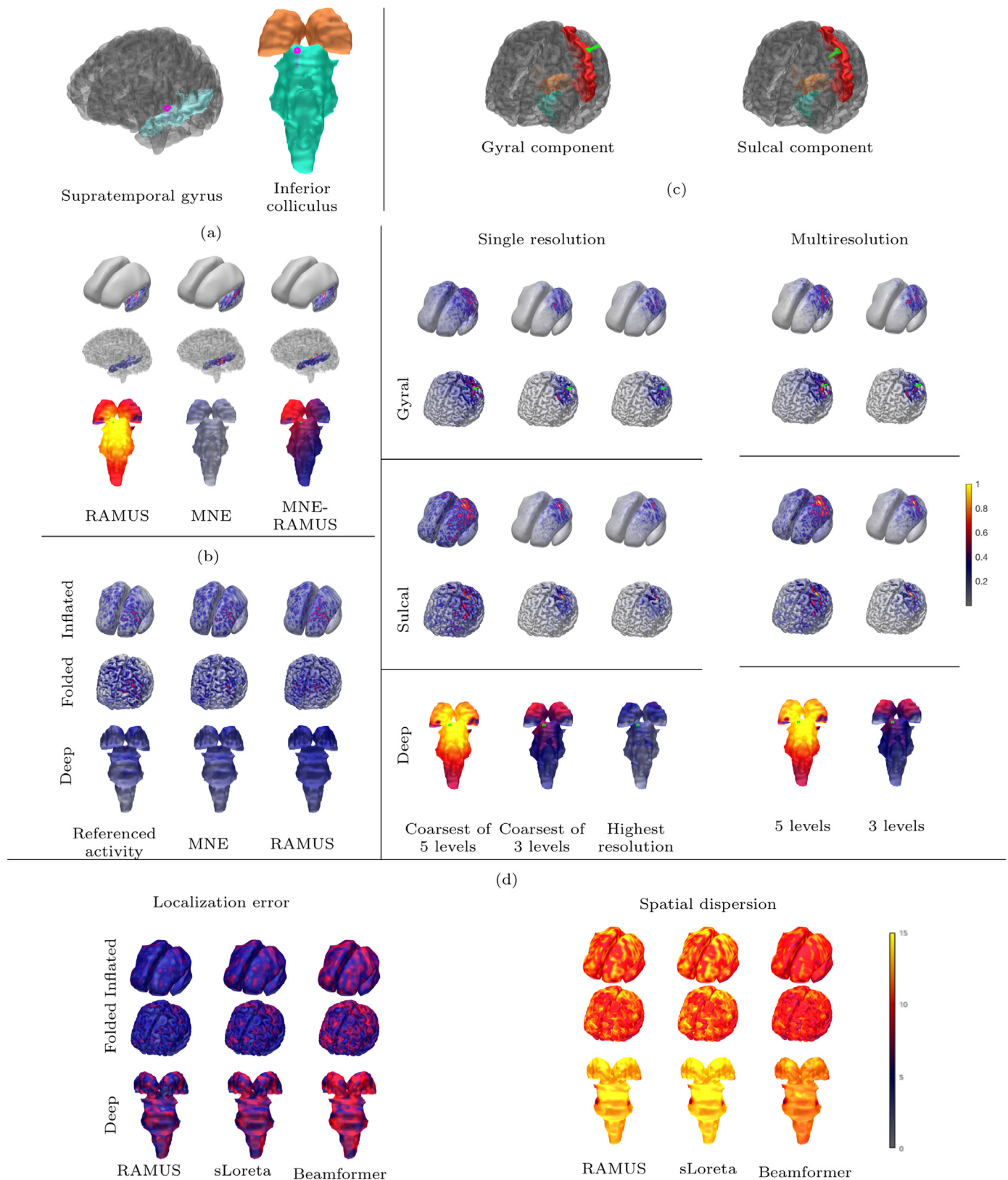
**Fig. A.6.** Complementary results obtained using the head model of subject (**I**). The synthetic source (magenta) (**on the left**) is located at supratemporal gyrus corresponding to auditory cortex and following synthetic source for deep structure located at *inferior colliculus*, posterior surface of brainstem. The synthetic source (green) is located at crown of postcentral gyrus (**on the right**) corresponding to the generator of the P22/N22 component. (a) illustrates the reconstructed activity with synthetic sources (shown in green) of auditory evoked simulated source on the left superior temporal gyrus for: RAMUS, MNE, and MNE-RAMUS, in which, the last technique associates with RAMUS using MNE instead of the IAS as the optimization algorithm. (b) shows the reconstructed activity for simulated source on the frontal left lobe by projecting and backprojecting and comparing the reconstructed activity via MNE and RAMUS with referenced activity. (c) demonstrates the performance of multiresolution RAMUS for cases of 5 and 3 levels compared to single resolution, i.e., the coarsest level of these. (d) depicts the mean source localization error and spatial dispersion for single source in millimeters to evaluate the performance of RAMUS compared to sLoreta and beamformer approaches. (For interpretation of the references to colour in this figure legend, the reader is referred to the web version of this article.)

In (c), the multiresolution effects of the RAMUS reconstruction are demonstrated for three numerically simulated dipolar sources placed in Fig. A.6): (i) post-central gyrus, (ii) posterior wall of the central sulcus, and (iii) posterior part of the upper brainstem. The multiresolution reconstructions obtained with 5 and 3 level decompositions are shown and compared to reconstructions corresponding to the coarsest level of these as well as the highest resolution. The results show that the intensity of the reconstructed subcortical activity is enhanced by the presence of coarse levels in the decomposition, whereas the high resolution levels strengthen the cortical part of the reconstruction and decrease the dispersion due to coarser levels. Comparing the multiresolution results to the case of the highest resolution, the dispersion increases as the number of resolution levels in the multiresolution decomposition grows.

Case (d) shows maps (see, e.g., Hauk et al., 2011) of the mean localization error and spatial dispersion obtained in the localization of a single source with RAMUS, sLORETA and UNGB. The localization error of RAMUS was suppressed compared to that of sLORETA and UNGB. The dispersion obtained with RAMUS was slightly elevated in comparison to UNGB and lowered compared to sLORETA.

## References

Allison, T., Wood, C.C., McCarthy, G., Spencer, D.D., 1991. Cortical somatosensory evoked potentials. II. Effects of excision of somatosensory or motor cortex in humans and monkeys. J. Neurophysiol. 66 (1), 64–82.

Aminoff, M., 2012. Aminoff's Electrodiagnosis in Clinical Neurology e-Book. Elsevier Health Sci. https://books.google.fi/books?id=ask7iOrvjJIC

Andersen, L.M., Jerbi, K., Dalal, S.S., 2020. Can EEG and MEG detect signals from the human cerebellum? NeuroImage 116817.

Antonakakis, M., Schrader, S., Wollbrink, A., Oostenveld, R., Rampp, S., Haueisen, J., Wolters, C.H., 2019. The effect of stimulation type, head modeling, and combined EEG and MEG on the source reconstruction of the somatosensory P20/N20 component. Hum. Brain Mapp. 40 (17), 5011–5028.

Attal, Y., Maess, B., Friederici, A., David, O., 2012. Head models and dynamic causal modeling of subcortical activity using magnetoencephalographic/electroencephalographic data. Rev. Neurosci. 23 (1), 85–95.

Attal, Y., Schwartz, D., 2013. Assessment of subcortical source localization using deep brain activity imaging model with minimum norm operators: a MEG study. PLoS One 8 (3), e59856.

Buchner, H., Adams, L., Müller, A., Ludwig, I., Knepper, A., Thron, A., Niemann, K., Scherg, M., 1995. Somatotopy of human hand somatosensory cortex revealed by dipole source analysis of early somatosensory evoked potentials and 3D-NMR tomography. Electroencephalogr. Clin. Neurophysiol./Evoked Potentials Section 96 (2), 121–134.

Buchner, H., Fuchs, M., Wischmann, H.-A., Dössel, O., Ludwig, I., Knepper, A., Berg, P., 1994. Source analysis of median nerve and finger stimulated somatosensory evoked potentials: multichannel simultaneous recording of electric and magnetic fields combined with 3D-MR tomography. Brain Topogr. 6 (4), 299–310.

Buchner, H., Knoll, G., Fuchs, M., Rienäcker, A., Beckmann, R., Wagner, M., Silny, J., Pesch, J., 1997. Inverse localization of electric dipole current sources in finite element models of the human head. Electroencephalogr. Clin. Neurophysiol. 102 (4), 267–278.

Buchner, H., Waberski, T., Fuchs, M., Wischmann, H.-A., Beckmann, R., Rienäcker, A., 1995. Origin of P16 median nerve SEP component identified by dipole source analysis-subthalamic or within the thalamo-cortical radiation? Exp. Brain Res. 104 (3), 511–518.

Buchner, H., Waberski, T.D., Fuchs, M., Drenckhahn, R., Wagner, M., Wichmann, H.A., 1996. Postcentral origin of P22: evidence from source reconstruction in a realistically shaped head model and from a patient with a postcentral lesion. Electroencephalogr. Clin. Neurophysiol./Evoked Potentials Section 100 (4), 332–342.

Calvetti, D., Hakula, H., Pursiainen, S., Somersalo, E., 2009. Conditionally Gaussian hypermodels for cerebral source localization. SIAM J. Imaging Sci. 2 (3), 879–909.

Cebolla, A.-M., Palmero-Soler, E., Dan, B., Chéron, G., 2011. Frontal phasic and oscillatory generators of the N30 somatosensory evoked potential. NeuroImage 54 (2), 1297–1306.

Chéron, G., Piette, T., Thiriaux, A., Jacquy, J., Godaux, E., 1994. Somatosensory evoked potentials at rest and during movement in Parkinson's disease: evidence for a specific apomorphine effect on the frontal N30 wave. Electroencephalogr. Clin. Neurophysiol./Evoked Potentials Section 92 (6), 491–501.

Connemann, B., Koehler, J., Presser, S., Hopf, H., 1999. Latency and amplitude variability in serial median nerve SEP recordings. Clin. Neurophysiol. 110 (9), 1664–1668.

Creutzfeldt, O., Fromm, G., Kapp, H., 1962. Influence of transcranial D-C currents on cortical neuronal activity. Exp. Neurol. 5, 436–452.

Cruccu, G., Aminoff, M., Curio, G., Guerit, J., Kakigi, R., Mauguiere, F., Rossini, P., Treede, R.-D., Garcia-Larrea, L., 2008. Recommendations for the clinical use of somatosensory-evoked potentials. Clin. Neurophysiol. 119 (8), 1705–1719.

Curio, G., Mackert, B.-M., Burghoff, M., Neumann, J., Nolte, G., Scherg, M., Marx, P., 1997. Somatotopic source arrangement of 600 Hz oscillatory magnetic fields at the human primary somatosensory hand cortex. Neurosci. Lett. 234 (2–3), 131–134.

Dalal, S.S., Osipova, D., Bertrand, O., Jerbi, K., 2013. Oscillatory activity of the human cerebellum: the intracranial electrocerebellogram revisited. Neurosci. Biobehav. Rev. 37 (4), 585–593.

Dannhauer, M., Lanfer, B., Wolters, C.H., Knösche, T.R., 2011. Modeling of the human skull in EEG source analysis. Hum. Brain Mapp. 32, 1383–1399.

Fried, S.J., Legatt, A.D., 2012. The utility of a forehead-to-inion derivation in recording the subcortical far-field potential (P14) during median nerve somatosensory-evoked potential testing. Clin. EEG Neurosci. 43 (2), 121–126.

Fried, S.J., Smith, D.M., Legatt, A.D., 2014. Median nerve somatosensory evoked potential monitoring during carotid endarterectomy: does reference choice matter? J. Clin. Neurophysiol. 31 (1), 55–57.

Fuchs, M., Wagner, M., Wischmann, H.-A., Köhler, T., Theißen, A., Drenckhahn, R., Buchner, H., 1998. Improving source reconstructions by combining bioelectric and biomagnetic data. Clin. Neurophysiol. 107 (2), 93–111.

Gobbelé, R., Buchner, H., Curio, G., 1998. High-frequency (600 Hz) sep activities originating in the subcortical and cortical human somatosensory system. Electroencephalogr. Clin. Neurophysiol./Evoked Potentials Section 108 (2), 182–189.

Götz, T., Huonker, R., Witte, O.W., Haueisen, J., 2014. Thalamocortical impulse propagation and information transfer in EEG and MEG. J. Clin. Neurophysiol. 31 (3), 253–260.

Gramfort, A., Kowalski, M., Hämäläinen, M., 2012. Mixed-norm estimates for the M/EEG inverse problem using accelerated gradient methods. Phys. Med. Biol. 57 (7), 1937.

Hämäläinen, M.S., Ilmoniemi, R.J., 1994. Interpreting magnetic fields of the brain: minimum norm estimates. Med. Biological Eng. Comput. 32 (1), 35–42.

Hari, R., Baillet, S., Barnes, G., Burgess, R., Forss, N., Gross, J., Hämäläinen, M., Jensen, O., Kakigi, R., Mauguière, F., et al., 2018. Ifcn-endorsed practical guidelines for clinical magnetoencephalography (MEG). Clin. Neurophysiol..

Hari, R., Hämäläinen, M., Joutsiniemi, S.L., 1989. Neuromagnetic steady-state responses to auditory stimuli. J. Acoust. Soc. Am. 86 (3), 1033–1039.

Hari, R., Puce, A., 2017. MEG-EEG Primer. Oxford University Press.

Hashimoto, I., Kimura, T., Tanosaki, M., Iguchi, Y., Sekihara, K., 2003. Muscle afferent inputs from the hand activate human cerebellum sequentially through parallel and climbing fiber systems. Clin. Neurophysiol. 114 (11), 2107–2117.

Haueisen, J., Leistritz, L., Süsse, T., Curio, G., Witte, H., 2007. Identifying mutual information transfer in the brain with differential-algebraic modeling: evidence for fast oscillatory coupling between cortical somatosensory areas 3B and 1. NeuroImage 37 (1), 130–136.

Hauk, O., Wakeman, D.G., Henson, R., 2011. Comparison of noise-normalized minimum norm estimates for MEG analysis using multiple resolution metrics. Neuroimage 54 (3), 1966–1974.

He, Q., Rezaei, A., Pursiainen, S., 2019. Zeffiro user interface for electromagnetic brain imaging: a GPU accelerated FEM tool for forward and inverse computations in matlab. Neuroinformatics 18 (2), 237–250.

Hoshiyama, M., Kakigi, R., 2001. Correspondence between short-latency somatosensory evoked brain potentials and cortical magnetic fields following median nerve stimulation. Brain Res. 908 (2), 140–148.

Hsieh, C.-L., Shima, F., Tobimatsu, S., Sun, S.-J., Kato, M., 1995. The interaction of the somatosensory evoked potentials to simultaneous finger stimuli in the human central nervous system. A study using direct recordings. Electroencephalogr. Clin. Neurophysiol./Evoked Potentials Section 96 (2), 135–142.

Jaiswal, A., Nenonen, J., Stenroos, M., Gramfort, A., Dalal, S.S., Westner, B.U., Litvak, V., Mosher, J.C., Schoffelen, J.-M., Witton, C., et al., 2020. Comparison of beamformer implementations for MEG source localization. NeuroImage 216, 116797.

Jones, E.G., 2001. The thalamic matrix and thalamocortical synchrony. Trends Neurosci. 24 (10), 595–601.

Jones, E.G., 2002. Thalamic circuitry and thalamocortical synchrony. Philos. Trans. R. Soc. Lond. Ser. B 357 (1428), 1659–1673.

Kaipio, J.P., Somersalo, E., 2004. Statistical and Computational Methods for Inverse Problems. Springer, Berlin.

Krishnaswamy, P., Obregon-Henao, G., Ahveninen, J., Khan, S., Babadi, B., Iglesias, J.E., Hämäläinen, M.S., Purdon, P.L., 2017. Sparsity enables estimation of both subcortical and cortical activity from MEG and EEG. Proc. Natl. Acad. Sci. 114 (48), E10465–E10474.

Laxton, A.W., Lozano, A.M., 2013. Deep brain stimulation for the treatment of alzheimer disease and dementias. World Neurosurg. 80 (3–4), S28–e1.

Lucka, F., Pursiainen, S., Burger, M., Wolters, C.H., 2012. Hierarchical Bayesian inference for the EEG inverse problem using realistic FE head models: depth localization and source separation for focal primary currents. NeuroImage 61 (4), 1364–1382.

Mauguière, F., Desmedt, J., Courjon, J., 1983. Neural generators of N18 and P14 far-field somatosensory evoked potentials studied in patients with lesion of thalamus or thalamo-cortical radiations. Electroencephalogr. Clin. Neurophysiol. 56 (4), 283–292.

Mauguière, F., Desmedt, J.E., 1989. Bilateral somatosensory evoked potentials in four patients with long-standing surgical hemispherectomy. Ann. Neurol. 26 (6), 724–731.

Miinalainen, T., Rezaei, A., Us, D., Nüßing, A., Engwer, C., Wolters, C.H., Pursiainen, S., 2019. A realistic, accurate and fast source modeling approach for the EEG forward problem. NeuroImage 184, 56–67.

Nakamura, A., Yamada, T., Goto, A., Kato, T., Ito, K., Abe, Y., Kachi, T., Kakigi, R., 1998. Somatosensory homunculus as drawn by MEG. Neuroimage 7 (4), 377–386.

Neugebauer, F., Möddel, G., Rampp, S., Burger, M., Wolters, C.H., 2017. The effect of head model simplification on beamformer source localization. Front. Neurosci. 11, 625.

Niedermeyer, E., da Silva, F.L., 2004. Electroencephalography: Basic Principles, Clinical Applications, and Related Fields. Lippincott Williams & Wilkins, Philadelphia.

Noël, P., Ozaki, I., Desmedt, J.E., 1996. Origin of N18 and P14 far-fields of median nerve somatosensory evoked potentials studied in patients with a brain-stem lesion. Electroencephalogr. Clin. Neurophysiol. 98 (2), 167–170.

Nuwer, M.R., 1998. Fundamentals of evoked potentials and common clinical applications today. Electroencephalogr Clin Neurophysiol 106 (2), 142–148.

Obeso, J.A., Marin, C., Rodriguez-Oroz, C., Blesa, J., Benitez-Temiño, B., Mena-Segovia, J., Rodríguez, M., Olanow, C.W., 2008. The basal ganglia in Parkinson's disease: current concepts and unexplained observations. Ann. Neurol. 64 (S2), S30–S46.

Pantev, C., Roberts, L.E., Elbert, T., Roß, B., Wienbruch, C., 1996. Tonotopic organization of the sources of human auditory steady-state responses. Hear. Res. 101 (1–2), 62–74.

Papadelis, C., Eickhoff, S.B., Zilles, K., Ioannides, A.A., 2011. BA3b and BA1 activate in a serial fashion after median nerve stimulation: direct evidence from combining source analysis of evoked fields and cytoarchitectonic probabilistic maps. Neuroimage 54 (1), 60–73.

Pascual-Marqui, R.D., et al., 2002. Standardized low-resolution brain electromagnetic tomography (sLORETA): technical details. Methods Find Exp. Clin. Pharmacol. 24 (Suppl D), 5–12.

Passmore, S.R., Murphy, B., Lee, T.D., 2014. The origin, and application of somatosensory evoked potentials as a neurophysiological technique to investigate neuroplasticity. J. Can. Chiropr. Assoc. 58 (2), 170.

Pierantozzi, M., Mazzone, P., Bassi, A., Rossini, P., Peppe, A., Altibrandi, M., Stefani, A., Bernardi, G., Stanzione, P., 1999. The effect of deep brain stimulation on the frontal N30 component of somatosensory evoked potentials in advanced Parkinson's disease patients. Clin. Neurophysiol. 110 (10), 1700–1707.

Pizzo, F., Roehri, N., Villalon, S.M., Trébuchon, A., Chen, S., Lagarde, S., Carron, R., Gavaret, M., Giusiano, B., McGonigal, A., et al., 2019. Deep brain activities can be detected with magnetoencephalography. Nat. Commun. 10 (1), 971.

Pursiainen, S., 2008. Coarse-to-fine reconstruction in linear inverse problems with application to limited-angle computerized tomography. J. Inverse Ill-Posed Probl. 16 (9), 873–886.

Pursiainen, S., 2012. Raviart–Thomas-type sources adapted to applied EEG and MEG: implementation and results. Inverse Probl. 28 (6), 065013.

Rezaei, A., Antonakakis, M., Piastra, M., Wolters, C.H., Pursiainen, S., 2020. Parametrizing the conditionally Gaussian prior model for source localization with reference to the P20/N20 component of median nerve SEP/SEF. Brain Sci. 10 (12), 934.

Rezaei, A., Koulouri, A., Pursiainen, S., 2020. Randomized multiresolution scanning in focal and fast E/MEG sensing of brain activity with a variable depth. Brain Topogr. 33 (2), 161–175.

Rice, J.K., Rorden, C., Little, J.S., Parra, L.C., 2013. Subject position affects EEG magnitudes. NeuroImage 64, 476–484.

Samuelsson, J.G., Khan, S., Sundaram, P., Peled, N., Hämäläinen, M.S., 2019. Cortical signal suppression (CSS) for detection of subcortical activity using MEG and EEG. Brain Topogr. 32 (2), 215–228.

Samuelsson, J.G., Sundaram, P., Khan, S., Sereno, M.I., Hämäläinen, M.S., 2020. Detectability of cerebellar activity with magnetoencephalography and electroencephalography. Hum. Brain Mapp. 41 (9), 2357–2372.

Schell, G.R., Strick, P.L., 1984. The origin of thalamic inputs to the arcuate premotor and supplementary motor areas. J. Neurosci. 4 (2), 539–560.

Schmidt, R., Thews, G., 1990. Physiologie des Menschen, 24. Auflage. Springer-Verlag, Berlin Heidelberg.

Seeber, M., Cantonas, L.-M., Hoevels, M., Sesia, T., Visser-Vandewalle, V., Michel, C.M., 2019. Subcortical electrophysiological activity is detectable with high-density EEG source imaging. Nat. Commun. 10 (1), 753.

Sekihara, K., Nagarajan, S.S., 2008. Adaptive Spatial Filters for Electromagnetic Brain Imaging. Springer Science & Business Media.

Sekihara, K., Nagarajan, S.S., Poeppel, D., Marantz, A., Miyashita, Y., 2001. Reconstructing spatio-temporal activities of neural sources using an MEG vector beamformer technique. IEEE Trans. Biomed. Eng. 48 (7), 760–771.

Shahid, S.S., Bikson, M., Salman, H., Wen, P., Ahfock, T., 2014. The value and cost of complexity in predictive modelling: role of tissue anisotropic conductivity and fibre tracts in neuromodulation. J. Neural Eng. 11 (3), 036002.

Sommariva, S., Sorrentino, A., 2014. Sequential Monte Carlo samplers for semi-linear inverse problems and application to magnetoencephalography. Inverse Probl. 30 (11), 114020.

Sonoo, M., Genba, K., Zai, W., Iwata, M., Mannen, T., Kanazawa, I., 1992. Origin of the widespread N18 in median nerve SEP. Electroencephalogr. Clin. Neurophysiol./Evoked Potentials Section 84 (5), 418–425.

Stühr, M., 2005. Somatosensible reizantworten von nerven, rückenmark und gehirn (SEP). Evozierte Potenziale. Springer. 21–252

Tadel, F., Baillet, S., Mosher, J.C., Pantazis, D., Leahy, R.M., 2011. Brainstorm: a user-friendly application for MEG/EEG analysis. Comput Intell. Neurosci. 8, 13.

Tesche, C., Karhu, J., 1997. Somatosensory evoked magnetic fields arising from sources in the human cerebellum. Brain Res. 744 (1), 23–31.

Tsuji, S., Shibasaki, H., Kato, M., Kuroiwa, Y., Shima, F., 1984. Subcortical, thalamic and cortical somatosensory evoked potentials to median nerve stimulation. Electroencephalogr. Clin. Neurophysiol./Evoked Potentials Section 59 (6), 465–476.

Tutorial 22: Source estimation, 2020. https://neuroimage.usc.edu/brainstorm/Tutorials/SourceEstimation, 2020.

Urasaki, E., Wada, S.-I., Kadoya, C., Yokota, A., Matsuoka, S., Shima, F., 1990. Origin of scalp far-field N18 of SSEPs in response to median nerve stimulation. Electroencephalogr. Clin. Neurophysiol./Evoked Potentials Section 77 (1), 39–51.

Van Veen, B.D., Van Drongelen, W., Yuchtman, M., Suzuki, A., 1997. Localization of brain electrical activity via linearly constrained minimum variance spatial filtering. IEEE Trans. Biomed. Eng. 44 (9), 867–880.